Aided Kalman Filter Models for GNSS-Based Space Navigation

Oliviero Vouch, *Graduate Student Member, IEEE*, Andrea Nardin, *Member, IEEE*, Alex Minetto, *Member, IEEE*, Simone Zocca, *Member, IEEE*, Matteo Valvano, and Fabio Dovis, *Member, IEEE*

***Abstract*—Ground-based assets traditionally aid space vehicle navigation, but the need for autonomy is steadily growing to meet the demands of future deep-space exploration. This paper proposes a customized Trajectory-Aware Extended Kalman Filter (TA-EKF) architecture, which conforms to the kinematic approach for Orbit Determination (OD) based on Global Navigation Satellite System (GNSS). Challenges at high altitudes, such as reduced GNSS signal availability and poor geometry, necessitate advanced filtering architectures leveraging external aiding data. When the receiver is not expected to interface with on-board guidance and control subsystems, *aiding observations*—in the form of a pre-mission planned spacecraft trajectory—allow to pursue precise and accurate OD only relying on GNSS measurements. Two alternative TA-EKF designs are formulated, which foresee *observation-domain* and *state-domain* integration of aiding observations, respectively. While the former design acts directly on the filter posterior, the latter aims to overcome deficiencies in the state prediction owing to misspecified process dynamics. The feasibility of using terrestrial GNSS signals in Earth-Moon transfer orbits (MTOs) is thus demonstrated against aiding observation errors and mismodeling. The developed TA-EKF models are thoroughly assessed via extensive Monte Carlo (MC) analyses, comparing their OD performance against a standalone EKF solution in a dedicated constellation simulator and mission planner.**

***Index Terms*—Global navigation satellite system, Moon, space service volume, Lunar missions, extended Kalman filter.**

I. Introduction

ALTHOUGH Global Navigation Satellite Systems (GNSSs) were historically conceived to supply accurate and dependable Positioning, Navigation and Timing (PNT) to terrestrial users, the momentum taken by the space sector has made the space environment a new playground for in-orbit GNSS-based navigation systems. Since the Global Positioning System Package (GPSPAC) onboard the Landsat 4 mission was launched in 1982 [1], major technology progress in GNSS space-borne receivers allowed to steadily improve the spectrum of PNT services within the Terrestrial Service Volume (TSV) [2]. Over the past decade, the increasing demand for navigation capability for space vehicles has fostered the expansion of the Space Service Volume (SSV) well beyond the Low-Earth Orbit (LEO) [3]. Interestingly, National Aeronautics and Space Administration (NASA) Magnetospheric Multiscale Mission (MMS) set the highest record for GNSS signal reception and onboard PNT to about 187 000 km, i.e., ∼29.3 Earth Radii (RE), away from the Earth's surface [4], [5].

At present, navigation, guidance and maneuvering of space vehicles is typically addressed by heavily relying on ground segment assets. Cutting-edge Orbit Determination (OD) techniques leverage Direct-to-Earth (DTE) radiometric tracking data from Deep Space Network (DSN) and employ complex off-board processing algorithms [6]. Sometimes, observations retrieved by the aid of a ground-based link are combined with relative radiometric and optimetric measurements retrieved on-board, thus affording a semi-autonomous navigation paradigm [7]. Similarly, maneuver control operations are typically accomplished via telecommands from ground stations [8], [9]. Despite achieving remarkably accurate OD and guidance, these approaches come with inherent drawbacks. High operational costs are put on the ground infrastructure, and fast exhaustion of tracking resources will likely happen as the number of missions increases. In addition, reliance on ground-based communication involves inherent limitations such as physical round-trip delays and data processing delays, which might prevent latency-critical operations from success [10], [11].

Increased autonomy from Earth-based tracking systems is thus crucial in spacecraft navigation subsystems to keep pace with the next decades of deep-space exploration both in terms of service availability and far-side accessibility [12]. Earth GNSS signals remain unquestionably pivotal for on-board autonomous navigation in transfer orbits as well as to assist in complex maneuvers such as trans-orbital injections or landings [13], [14]. Being GNSS satellite constellations conceived to only provide Earth coverage, the space environment

Manuscript received 31 January 2024; revised 10 May 2024; accepted 14 May 2024. Date of publication 21 May 2024; date of current version 17 June 2024. This work was supported by the ASI/Politecnico di Torino "Attività di R&S inerente alla Navigazione GNSS nello Space volume Terra/Luna nell'ambito del Lunar GNSS Receiver Experiment." under Contract 2021-26-HH.0. The work of Oliviero Vouch was supported by the Politecnico di Torino Interdepartmental Centre for Service Robotics (PIC4SeR). The work of Alex Minetto was supported by the Programma Operativo Nazionale (PON) Ricerca ed Innovazione of the Italian Ministry of University and Research (MUR) under Contract 32-G-13427-5 DM 1062/2021. *(Corresponding author: Oliviero Vouch.)*

Oliviero Vouch, Andrea Nardin, Alex Minetto, Simone Zocca, and Fabio Dovis are with the Department of Electronics and Telecommunications, Politecnico di Torino, 10129 Turin, Italy (e-mail: oliviero.vouch@polito.it; andrea.nardin@polito.it; alex.minetto@polito.it; simone.zocca@polito.it; fabio.dovis@polito.it).

Matteo Valvano was with the Department of Electronics and Telecommunications, Politecnico di Torino, 10129 Turin, Italy. He is now with Intecs R&D AeroSpace division, Intecs Solutions S.p.A., 00131 Rome, Italy (e-mail: matteo.valvano@intecs.it).

Digital Object Identifier 10.1109/JRFID.2024.3403914

poses non-trivial challenges that can hinder performance of space-borne GNSS receiving terminals. First, reduced GNSS signal availability is likely to be experienced at high altitudes because of the very-limited region in the field of view where satellites can be observed [15]. In addition, the unfortunate distribution of GNSS constellations increases the linear dependency of the retrieved satellite measurements, thus resulting in very-high Geometric Dilution Of Precision (GDOP) when combined in multilateration solutions. In such a context, it is worth mentioning that several space agencies are actively proposing dedicated and scalable lunar-centric communication and navigation infrastructures; this will benefit the breadth of lunar-orbiting and surface assets through empowering PNT capabilities [16].

In order to pursue ground-segment independent yet precise OD using GNSS signals, the well-documented dynamic approach to precise OD considers to combine the standalone GNSS state-estimation filter with a mathematical model of orbital dynamics [17]. This orbital propagator, which acts as a dead-reckoning sensor based on known physics of orbital motion, is useful both to constrain the coarse GNSS-only PNT solutions and to bridge position fixing gaps (e.g., if fewer than four satellites are available and a batch estimator is employed). The resulting hybrid architecture is often referred to as Orbital Filter (OF), as first introduced by a pioneer study on the design of an Extended Kalman Filter (EKF) algorithm for GNSS-based OD in Earth-Moon transfer orbits (MTOs) [18]. Alternatively, deterministic process dynamics in the state-estimation filter can be characterized via a reduced dynamic orbital model [19]. Then, flaws in the orbital model are captured by augmenting the process model with stochastic components (a.k.a., empirical accelerations). First adopted in the Global Positioning System (GPS) demonstration receiver for the TOPEX/Poseidon mission [20], this approach has been later resumed in the context of MTO navigation [21]. However, the augmented state-space reflecting the integration of an orbital model as part of the state dynamics increases the computational load; this might be a concern given the limited computational resources on-board a spacecraft. Moreover, these architectures require deterministic a-priori information (e.g., control inputs from Guidance, Navigation & Control (GNC) subsystems) to accomplish optimal process state propagation.

As opposed to these and other approaches, this study attempts to demonstrate the feasibility of GNSS-based OD under the operational assumption that the state-estimation filter has access to minimal amount of a-priori information about process dynamics. This assumption finds tangible application in the design of the GNSS receiver involved in the upcoming Lunar GNSS Receiver Experiment (LuGRE) mission. Such a scientific mission is based on a joint NASA-Italian Space Agency (ASI) demonstration payload which will be carried on the Firefly Blue Ghost Mission 1 (BGM1) with the goal of demonstrating multi-GNSS-based PNT in cis-lunar space and at Moon altitudes [22], [23]. The LuGRE GNSS receiver is not expected to interface with the spacecraft GNC subsystem while only relying on GNSS observables and aiding data (i.e., GNSS ephemeris and planned spacecraft trajectory) provided from its ground segment. Among the driving scientific investigations identified to respond to the LuGRE objectives, it is considered the performance assessment of filtering-based PNT solutions obtained both onboard throughout the mission and via ground-based post-processing of the multi-GNSS observables collected throughout MTO up to Moon altitudes (i.e., about 62 RE) [24], [25], [26].

In light of the foregoing, this contribution addresses the problem of GNSS-based spacecraft navigation adopting a kinematic approach [27] which best fit with the operational assumption for missions such as the aforementioned LuGRE, although the proposed methodology can effectively accommodate more sophisticated physical models of orbital motion. As such, a plain formulation of an EKF filter with oversimplified constant-velocity process dynamics is considered. Then, aiding information in the form of a pre-mission planned spacecraft trajectory—loaded as a configuration file in the spacecraft microprocessor board—is leveraged to enhance the filter posterior estimate. The developed aided architecture, namely a Trajectory-Aware EKF (TA-EKF), envisages two alternative designs to accommodate spacecraft-state observations (i.e., *aiding observations*) in the state-estimation filter. On the one hand, these aiding observations can be integrated in the filter measurement model by augmenting the observables' set; hence, an *observation-domain integration* is pursued. On the other hand, aiding observations can be optimally combined with the time-propagated estimate to overcome deficiencies in the state prediction owing to neglected orbital dynamics; in this case, a *state-domain integration* is pursued. These contributions significantly extend our previous work in [28] with the rigorous formulation and the extensive analysis of two alternative designs of aided EKF-based models tailored to GNSS-based PNT in MTOs.

The developed TA-EKF architectures offer multiple advantages. First, they can enable GNSS-based OD with minimal amount of a-priori process information, thus not requiring integration of external input controls from onboard GNC subsystems. Moreover, the adoption of a simplified model for state dynamics represents an attractive alternative to resource-intensive designs of filtering-based estimators embedding complex physical models. By leveraging a dedicated mission planner and constellation simulator which can reproduce the geometry of GNSS constellations and the observables retrieved throughout MTOs, Monte Carlo (MC) analyses are first conducted to exhaustively investigate both TA-EKF variants and highlight their equivalent accuracy performance for the OD task. In particular, a standalone EKF-based solution is considered as benchmark to show the limited navigation performance achievable with a standalone kinematic approach. Then, corrupted aiding observations mismatched with the traveled orbit profile are introduced in order to asses the navigation accuracy loss incurred by the TA-EKF models.

The subsequent sections of this paper are organized as follows. Section II provides a technical background on statistical state estimation within the framework of the EKF. Section III introduces the proposed TA-EKF estimation filters, and Section IV delineates the simulation framework employed to replicate the navigation conditions for a target mission-case

scenario of GNSS-based PNT in MTO. Then, a thorough analysis of filter performances is presented in Section V. Finally, Section VI encapsulates the drawn conclusions.

II. Background

In the framework of filtering-based statistical estimation, the process to be estimated and the associated dependency of measurements may be written in the form [29]:

$$\boldsymbol{x}_k = \boldsymbol{f}_{k-1}\left(\boldsymbol{x}_{k-1}, \boldsymbol{c}_{d,k-1}\right) + \boldsymbol{w}_{k-1} \tag{1}$$

$$\boldsymbol{z}_k = \boldsymbol{h}_k(\boldsymbol{x}_k) + \boldsymbol{v}_k \tag{2}$$

where:

- $\boldsymbol{x}_k$ is the true, unknown process state at time t_k;
- $\boldsymbol{z}_k$ is the measurement vector at time t_k;
- $\boldsymbol{w}_{k-1} \sim \mathcal{N}(\boldsymbol{0}, \boldsymbol{Q}_{k-1})$ and $\boldsymbol{v}_k \sim \mathcal{N}(\boldsymbol{0}, \boldsymbol{R}_k)$ are the normally distributed process and measurement noises, respectively; they are assumed with zero-mean, known variance-covariance statistics and mutually independent.
- $\boldsymbol{f}_{k-1}$ and $\boldsymbol{h}_k$ are known, non-linear state-transition and observation functions, respectively.
- $\boldsymbol{c}_{d,k-1}$ are deterministic forcing inputs (e.g., thrust acceleration) affecting the process state.

Given that the current study assumes the GNSS receiver not to have access to external controls from onboard GNC subsystems, these terms are assumed equal to zero in the following.

The combination of (1) and (2) leads to a state-space formulation following a Hidden Markov Model (HMM) [30]. Identifying with $\boldsymbol{x}_k^*$ the estimated process state at time t_k—which includes, among the other quantities, the spacecraft trajectory—the following relation holds:

$$\boldsymbol{x}_k = \boldsymbol{x}_k^* + \Delta\boldsymbol{x}_k \tag{3}$$

which introduces $\Delta\boldsymbol{x}_k$ as the residual of the estimate. Choosing $\boldsymbol{x}_k^* = \boldsymbol{f}_{k-1}(\boldsymbol{x}_{k-1}^*)$, the linear(-ized) process dynamics and measurement models can be obtained in terms of residuals [29]:

$$\Delta\boldsymbol{x}_k = \boldsymbol{\Phi}_{k-1} \cdot \Delta\boldsymbol{x}_{k-1} + \boldsymbol{w}_{k-1} \tag{4}$$

$$\boldsymbol{z}_k - \boldsymbol{h}_k\left(\boldsymbol{x}_k^*\right) = \boldsymbol{H}_k \cdot \Delta\boldsymbol{x}_k + \boldsymbol{v}_k \tag{5}$$

where $\boldsymbol{\Phi}_{k-1}$ and $\boldsymbol{H}_k$ are the linear(-ized) state-transition matrix and measurement matrix, respectively. Based on model (4), the predicted residual takes the form:

$$\Delta\hat{\boldsymbol{x}}_k^- = \boldsymbol{\Phi}_{k-1} \cdot \Delta\hat{\boldsymbol{x}}_{k-1} \tag{6}$$

being $\Delta\hat{\boldsymbol{x}}_{k-1}$ the residual on the last process estimate at t_{k-1}. Summing $\boldsymbol{x}_k^*$ on both sides of (6), the linear(-ized) process prediction model in terms of total states reads as [29]:

$$\underbrace{\boldsymbol{x}_{\boldsymbol{k}}^{\boldsymbol{*}} + \Delta\hat{\boldsymbol{x}}_{\boldsymbol{k}}^{\boldsymbol{-}}}_{\hat{\boldsymbol{x}}_{\boldsymbol{k}}^{\boldsymbol{-}}} = \boldsymbol{\Phi}_{k-1} \cdot \left(\underbrace{\boldsymbol{x}_{k-1}^* + \Delta\hat{\boldsymbol{x}}_{k-1}}_{\hat{\boldsymbol{x}}_{k-1}} \right) \tag{7}$$

with the associated predicted process covariance:

$$\boldsymbol{P}_k^- = \boldsymbol{\Phi}_{k-1}\boldsymbol{P}_{k-1}\boldsymbol{\Phi}_{k-1}^T + \boldsymbol{Q}_k. \tag{8}$$

Accordingly, leveraging on model (5), the corrected residual estimate at time t_k follows as:

$$\Delta\hat{\boldsymbol{x}}_{\boldsymbol{k}} = \Delta\hat{\boldsymbol{x}}_k^- + \boldsymbol{K}_k \left[\boldsymbol{z}_k - \underbrace{\left(\boldsymbol{h}_k\left(\boldsymbol{x}_k^*\right) + \boldsymbol{H}_k\Delta\hat{\boldsymbol{x}}_{\boldsymbol{k}}^{\boldsymbol{-}}\right)}_{\hat{\boldsymbol{z}}_{\boldsymbol{k}}^{\boldsymbol{-}}} \right] \tag{9}$$

where $\boldsymbol{K}_k = \boldsymbol{P}_k^-\boldsymbol{H}_k^T(\boldsymbol{H}_k\boldsymbol{P}_k^-\boldsymbol{H}_k^T + \boldsymbol{R}_k)^{-1}$ is the Kalman gain. The predicted measurements $\hat{\boldsymbol{z}}_k^-$ are highlighted.

Eventually, the linear(-ized) process update equation in terms of total states is obtained from (9) by resuming $\boldsymbol{x}_k^*$ [29]:

$$\underbrace{\boldsymbol{x}_{\boldsymbol{k}}^{\boldsymbol{*}} + \Delta\hat{\boldsymbol{x}}_{\boldsymbol{k}}}_{\hat{\boldsymbol{x}}_{\boldsymbol{k}}} = \hat{\boldsymbol{x}}_k^- + \boldsymbol{K}_k\left(\boldsymbol{z}_k - \hat{\boldsymbol{z}}_{\boldsymbol{k}}^{\boldsymbol{-}}\right). \tag{10}$$

The associated process covariance update is:

$$\boldsymbol{P}_k = (\boldsymbol{I} - \boldsymbol{K}_k\boldsymbol{H}_k)\boldsymbol{P}_k^-(\boldsymbol{I} - \boldsymbol{K}_k\boldsymbol{H}_k)^T + \boldsymbol{K}_k\boldsymbol{R}_k\boldsymbol{K}_k^T. \tag{11}$$

A. Transitional Model for Process Dynamics

Although a plethora of possibilities exist [31], a simple constant velocity model is selected to characterize the discrete-time evolution of the process state. Then, the state vector at time t_k is defined as:

$$\boldsymbol{x}_k = \left[\boldsymbol{r}_k\ \dot{\boldsymbol{r}}_k\ b_k\ \dot{b}_k\right]^T \tag{12}$$

and it involves the following quantities:

- $\boldsymbol{r}_k = [x_k\, y_k\, z_k]$ the spacecraft antenna absolute position vector in (m);
- $\dot{\boldsymbol{r}}_k = [\dot{x}_k\, \dot{y}_k\, \dot{z}_k]$ the spacecraft antenna absolute velocity vector in (m/s);
- b_k the range equivalent of the GNSS receiver clock offset in (m);
- $\dot{b}_k$ the range-rate equivalent of the GNSS receiver clock drift in (m/s);

Based on (12), the state-transition matrix corresponds to [32]:

$$\boldsymbol{\Phi}_{k-1} = \begin{bmatrix} \boldsymbol{I}_{3\times3} & \boldsymbol{I}_{3\times3}\Delta t & \boldsymbol{0}_{3\times1} & \boldsymbol{0}_{3\times1} \\ \boldsymbol{0}_{3\times3} & \boldsymbol{I}_{3\times3} & \boldsymbol{0}_{3\times1} & \boldsymbol{0}_{3\times1} \\ \boldsymbol{0}_{1\times3} & \boldsymbol{0}_{1\times3} & 1 & \Delta t \\ \boldsymbol{0}_{1\times3} & \boldsymbol{0}_{1\times3} & 0 & 1 \end{bmatrix} \tag{13}$$

where Δt is the process state propagation interval, $\boldsymbol{I}_{n\times n}$ is the $n \times n$ identity matrix and $\boldsymbol{0}_{n\times n}$ is the $n \times n$ null-matrix. Eventually, the process noise variance-covariance matrix can be compactly written as [32]:

$$\boldsymbol{Q}_{k-1} = \begin{bmatrix} \boldsymbol{Q}_p & \boldsymbol{0}_{6\times2} \\ \boldsymbol{0}_{2\times6} & \boldsymbol{Q}_t \end{bmatrix} \tag{14}$$

where $\boldsymbol{Q}_p$ is the covariance component for the positioning states resolved about the Earth-Centred Earth-Fixed (ECEF)-frame axes; it reads as:

$$\boldsymbol{Q}_p = \begin{bmatrix} \frac{\Delta t^3}{3} & \frac{\Delta t^2}{2} \\ \frac{\Delta t^2}{2} & \Delta t \end{bmatrix} \otimes \operatorname{diag}\left(\underbrace{S_{a,x}, S_{a,y}, S_{a,z}}_{S_a} \right) \tag{15}$$

being $\boldsymbol{S}_a$ the acceleration Power Spectral Density (PSD) and $\otimes$ the Kronecker product. Similarly, $\boldsymbol{Q}_t$ is the covariance component for the timing states and equals:

$$\boldsymbol{Q}_t = \begin{bmatrix} S_{c\phi}\Delta t + S_{cf}\dfrac{\Delta t^3}{3} & S_{cf}\dfrac{\Delta t^2}{2} \\ S_{cf}\dfrac{\Delta t^2}{2} & S_{cf}\Delta t \end{bmatrix} \tag{16}$$

being $S_{c\phi}$ and S_{cf} the PSDs of the GNSS receiver clock phase-drift and frequency-drift, respectively.[1]

III. Trajectory-Aware EKF

In the proposed TA-EKF architecture, the aiding information integrated in the GNSS-based navigation filter is conveyed as observations having a functional relationship with the spacecraft kinematic state; the latter is usually meant in terms of instantaneous position and velocity of the orbiting probe. In the context of this application, these aiding observations are available to the filtering-based estimator from a pre-mission designed spacecraft orbit. This trajectory, which includes the spacecraft kinematic state for the entire mission span, can be obtained via a high-precision, physics-based orbit propagator embedding models of gravitational effects from celestial bodies, atmospheric drag, solar radiation pressure and possibly models of thrusting maneuvers [34]. Nevertheless, ground-dependent subsystems (e.g., ground-based networks for radiometric measurements) must also be regarded among the means aiding observations are most commonly retrieved from.

Aiding observations can be profitably fused in the GNSS-based filter as soon as a new set of locally estimated satellite measurements is available. Specifically, two alternative configurations for aiding data integration are proposed in Fig. 1, and their discussion is the content that follows.

A. Observation-Domain Aiding Integration

By interpreting the aiding observations as a measurement vector $\tilde{\boldsymbol{z}}_k$ with a known functional dependence on the state, they can augment the observables set and fit into the measurement model (2) according to the following relation:

$$\tilde{\boldsymbol{z}}_k = \tilde{\boldsymbol{h}}_k(\boldsymbol{x}_k) + \boldsymbol{\zeta}_k \tag{17}$$

$\tilde{\boldsymbol{h}}_k$ being the known (and possibly non-linear) measurement function for the aiding observations and $\boldsymbol{\zeta}_k \sim \mathcal{N}(\boldsymbol{0}, \tilde{\boldsymbol{R}}_k)$ being the corresponding normally-distributed nuisance term.

Assuming $\tilde{\boldsymbol{h}}_k$ linear(-izable), (23) can be written as:

$$\tilde{\boldsymbol{z}}_k = \tilde{\boldsymbol{H}}_k\boldsymbol{x}_k + \boldsymbol{\zeta}_k \tag{18}$$

and the linear(-ized) measurement model (5) can therefore be augmented to embed the aiding observations as follows:

$$\begin{bmatrix} \boldsymbol{z}_k - \boldsymbol{h}_k(\boldsymbol{x}_k^*) \\ \tilde{\boldsymbol{z}}_k - \tilde{\boldsymbol{h}}_k(\boldsymbol{x}_k^*) \end{bmatrix} = \begin{bmatrix} \boldsymbol{H}_k \\ \tilde{\boldsymbol{H}}_k \end{bmatrix} \cdot \Delta\boldsymbol{x}_k + \begin{bmatrix} \boldsymbol{v}_k \\ \boldsymbol{\zeta}_k \end{bmatrix}. \tag{19}$$

As mentioned earlier, in this research the aiding observations are available in terms of a planned orbit through pre-mission design; hence, they do not bring any information about the GNSS receiver clock offset and drift states. It follows that the aiding observations at time t_k can be defined as follows:

$$\tilde{\boldsymbol{z}}_k = \begin{bmatrix} \underbrace{\tilde{x}_k\,\tilde{y}_k\,\tilde{z}_k}_{\tilde{\boldsymbol{r}}_k}\,\underbrace{\dot{\tilde{x}}_k\,\dot{\tilde{y}}_k\,\dot{\tilde{z}}_k}_{\dot{\tilde{\boldsymbol{r}}}_k} \end{bmatrix}^T \tag{20}$$

where $\tilde{\boldsymbol{r}}_k$ and $\dot{\tilde{\boldsymbol{r}}}_k$ are, respectively, the position and velocity aiding states (i.e., spacecraft instantaneous kinematic states). Hence, they admit a simple, linear relationship with the state $\boldsymbol{x}_k$:

$$\begin{bmatrix} \tilde{\boldsymbol{r}}_k\,\dot{\tilde{\boldsymbol{r}}}_k \end{bmatrix}^T = [\boldsymbol{r}_k\,\dot{\boldsymbol{r}}_k]^T + \boldsymbol{\zeta}_k \tag{21}$$

which brings to the following definition of the aiding observation function in state-space form:

$$\tilde{\boldsymbol{h}}_k(\boldsymbol{x}_k) = \begin{bmatrix}\boldsymbol{I}_{6\times6}\ \boldsymbol{0}_{6\times2}\end{bmatrix}\boldsymbol{x}_k = \tilde{\boldsymbol{H}}_k\boldsymbol{x}_k. \tag{22}$$

Noticeably, in this case $\tilde{\boldsymbol{h}}_k$ is a linear function. Hence, the observation matrix $\tilde{\boldsymbol{H}}_k$ is derived without approximations and can readily fit into model (19).

It is worth stressing that appropriate modeling of the aiding variance-covariance statistics through $\tilde{\boldsymbol{R}}_k$ is mandatory to adopt this strategy in a Kalman estimator. In principle, these variances should be finely tuned according to the thoroughness of the source delivering aiding observations (e.g., how sophisticated the physics-based propagator in the software suite for orbit design and maneuver planning is [34]). However, absence of this information can be assumed. If so, $\tilde{\boldsymbol{R}}_k$ is meant to model the degree of trust the estimator puts on the source aiding observations are retrieved from. Alternatively, it might be designed based on a set of pre-mission requirements allocated to the external aiding source. Furthermore, independence between GNSS observables (e.g., pseudoranges, pseudorange

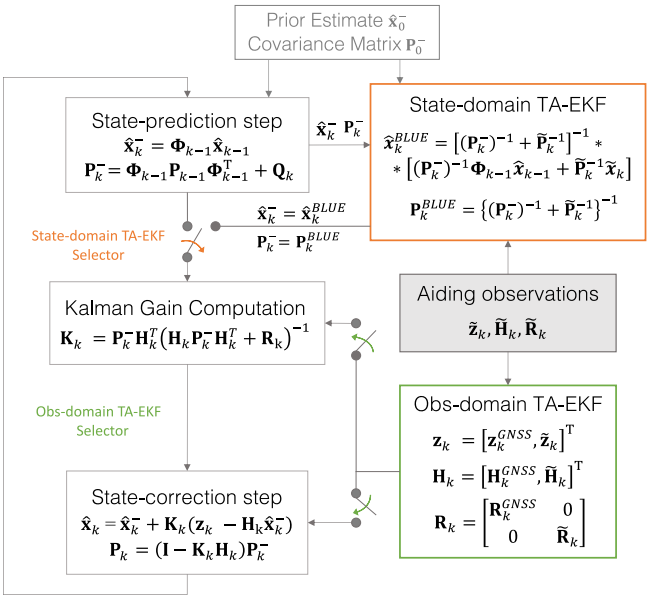

Fig. 1. Processing stages of the developed TA-EKF model for both state-domain (orange) and observation-domain (green) architectures. Aiding observations are highlighted with gray-colored background.

[1]For $\boldsymbol{Q}_{k-1}$, $S_{c\phi} = 2.5 \cdot 10^{-12}\,(\mathrm{m/s})^2/\mathrm{Hz}$, $S_{cf} = 1.5 \cdot 10^{-4}\,(\mathrm{m/s^2})^2/\mathrm{Hz}$, $S_{a,x} = S_{a,y} = S_{a,z} = 2\,(\mathrm{m/s^2})^2/\mathrm{Hz}$ were set as in [33].

rate measurements) and aiding observations can be safely assumed when the latter result from a pre-mission orbital planning. Similarly, when aiding information is obtained through ground-based assets, the complex processing performed at the ground segment inherently decorrelates such observations from GNSS measurements estimated on-board.

B. State-Domain Aiding Integration

As an alternative approach to the integration of aiding data in the observation model, the information carried by the aiding observations can be fused into the dynamical model prior to the integration of GNSS measurements. The aim of this design choice is to profitably leverage aiding information to empower a transitional model based on simplistic constant-velocity assumptions. In such sense, two estimates of the unknown state have to be optimally combined at time t_k:

- a time-propagated estimate $\hat{\boldsymbol{x}}_k^- = \boldsymbol{\Phi}_{k-1}\hat{\boldsymbol{x}}_{k-1}$ yielded by the transitional model;
- an *aiding state* $\tilde{\boldsymbol{x}}_k$ yielded by the aiding observations $\tilde{\boldsymbol{z}}_k$.

From (18), the Weighted Least-Squares (WLS) estimate of the aiding state can be obtained as:

$$\tilde{\boldsymbol{x}}_k = \left(\tilde{\boldsymbol{H}}_k^\top \tilde{\boldsymbol{R}}_k^{-1} \tilde{\boldsymbol{H}}_k\right)^{-1} \tilde{\boldsymbol{H}}_k^\top \tilde{\boldsymbol{R}}_k^{-1} \tilde{\boldsymbol{z}}_k. \tag{23}$$

The essence of state-domain integration lies in recognizing the assumption that both estimates come as realizations of normally distributed multivariate random variables with a common mean—the true, unknown process state $\boldsymbol{x}_k$—and different variance-covariance matrices. For the time-propagated state, the variance-covariance $\boldsymbol{P}_k^-$ is given in (8). For the aiding state, instead, it can be computed as the variance-covariance of the WLS estimate:

$$\tilde{\boldsymbol{P}}_k = \left(\tilde{\boldsymbol{H}}_k^\top \tilde{\boldsymbol{R}}_k^{-1} \tilde{\boldsymbol{H}}_k\right)^{-1} \tag{24}$$

which propagates the aiding observations covariance $\tilde{\boldsymbol{R}}_k$ in the aiding state (the reader is invited to refer to (43) in the Appendix). In light of the above and adopting a Generalized Least-Squares (GLS) approach, the following loss function can be defined:

$$\begin{aligned} &L(\boldsymbol{x}_{k,\text{est}}\boldsymbol{x}_k, \boldsymbol{P}_k^-, \tilde{\boldsymbol{P}}_k) \\ &\quad = (\boldsymbol{x}_{k,\text{est}} - \boldsymbol{x}_k)^T((\boldsymbol{P}_k^-)^{-1} + \tilde{\boldsymbol{P}}_k^{-1})(\boldsymbol{x}_{k,\text{est}} - \boldsymbol{x}_k) \end{aligned} \tag{25}$$

where $\boldsymbol{x}_{k,\text{est}}$ is the estimate of $\boldsymbol{x}_k$ considered to evaluate the loss. As a matter of fact, (25) corresponds to the square of their Mahalanobis distance. Then, the Best Linear Unbiased estimator (BLUE) of the common mean [35], [36], [37] which minimizes (25) can be obtained as:

$$\hat{\boldsymbol{x}}_k^{BLUE} = \left[\left(\boldsymbol{P}_k^-\right)^{-1} + \tilde{\boldsymbol{P}}_k^{-1}\right]^{-1}\left[\left(\boldsymbol{P}_k^-\right)^{-1}\boldsymbol{\Phi}_{k-1}\hat{\boldsymbol{x}}_{k-1} + \tilde{\boldsymbol{P}}_k^{-1}\tilde{\boldsymbol{x}}_k\right]. \tag{26}$$

To compute the covariance of $\hat{\boldsymbol{x}}_k^{BLUE}$ it is convenient to resort to the uncertainty propagation principles for linear combinations. Assuming independence among the random vectors $\boldsymbol{\Phi}_{k-1}\hat{\boldsymbol{x}}_{k-1}$ and $\tilde{\boldsymbol{x}}_k$, it can be shown that

$$\boldsymbol{P}_k^{BLUE} = \left\{\left(\boldsymbol{P}_k^-\right)^{-1} + \tilde{\boldsymbol{P}}_k^{-1}\right\}^{-1}. \tag{27}$$

The interested reader can refer to the Appendix section for a full derivation of (27).

Taking the common-mean estimate $\hat{\boldsymbol{x}}_k^{BLUE}$ as the optimal combination between the time-propagated estimate and the aiding state, it can then be used to enhance the EKF prediction step by setting $\hat{\boldsymbol{x}}_k^- = \hat{\boldsymbol{x}}_k^{BLUE}$ and $\boldsymbol{P}_k^- = \boldsymbol{P}_k^{BLUE}$.

1) The Case of Diagonal Covariance Matrices: When both the aiding states and the time-propagated state have i.i.d. components (i.e., the multivariate normal distribution is equivalent to the product of the univariates for each state dimension), the variance-covariance matrices $\boldsymbol{P}_k^-$ and $\tilde{\boldsymbol{P}}_k$ are diagonal. In such a case, the state-domain formulation for aiding integration can be simplified to yield a more compact representation. In fact, provided that both $\boldsymbol{P}_k^-$ and $\tilde{\boldsymbol{P}}_k$ have non-zero diagonal elements, the inverse matrices are given by replacing each main diagonal elements by its reciprocal. By relying on this property, it is easy to verify that (26) can be simplified to

$$\hat{\boldsymbol{x}}_k^{BLUE} = \boldsymbol{V}_k\boldsymbol{\Phi}_{k-1}\hat{\boldsymbol{x}}_{k-1} + \boldsymbol{W}_k\tilde{\boldsymbol{x}}_k \tag{28}$$

where

$$\boldsymbol{V}_k = \begin{bmatrix} \alpha_{k,1} & 0 & \cdots & 0 \\ 0 & \alpha_{k,2} & \cdots & 0 \\ \vdots & \vdots & \ddots & \\ 0 & 0 & & \alpha_{k,8} \end{bmatrix} \tag{29}$$

$$\boldsymbol{W}_k = \begin{bmatrix} \beta_{k,1} & 0 & \cdots & 0 \\ 0 & \beta_{k,2} & \cdots & 0 \\ \vdots & \vdots & \ddots & \\ 0 & 0 & & \beta_{k,8} \end{bmatrix} \tag{30}$$

$$\alpha_{k,i} = \frac{\left(\boldsymbol{P}_k^-\right)_{i,i}^{-1}}{\left(\boldsymbol{P}_k^-\right)_{i,i}^{-1} + \left(\tilde{\boldsymbol{P}}_k\right)_{i,i}^{-1}} \tag{31}$$

and

$$\beta_{k,i} = \frac{\left(\tilde{\boldsymbol{P}}_k\right)_{i,i}^{-1}}{\left(\boldsymbol{P}_k^-\right)_{i,i}^{-1} + \left(\tilde{\boldsymbol{P}}_k\right)_{i,i}^{-1}}. \tag{32}$$

Equation (28) is a weighted arithmetic mean of the time-propagated state and the aiding state with variance-defined weights. This weighted mean is the maximum likelihood estimator of the mean of the probability distributions of the two vectors under the assumption that they are mutually independent and normally distributed with the same mean and that each state variable is uncorrelated from the others [38].

From (27) it is also straightforward to derive a model for the covariance matrix of (28), which results in

$$\boldsymbol{P}_k^{BLUE} = \begin{bmatrix} \gamma_{k,1} & 0 & \cdots & 0 \\ 0 & \gamma_{k,2} & \cdots & 0 \\ \vdots & \vdots & \ddots & \\ 0 & 0 & & \gamma_{k,8} \end{bmatrix} \tag{33}$$

where

$$\gamma_{k,i} = \frac{1}{\left(\boldsymbol{P}_k^-\right)_{i,i}^{-1} + \left(\tilde{\boldsymbol{P}}_k\right)_{i,i}^{-1}}. \tag{34}$$

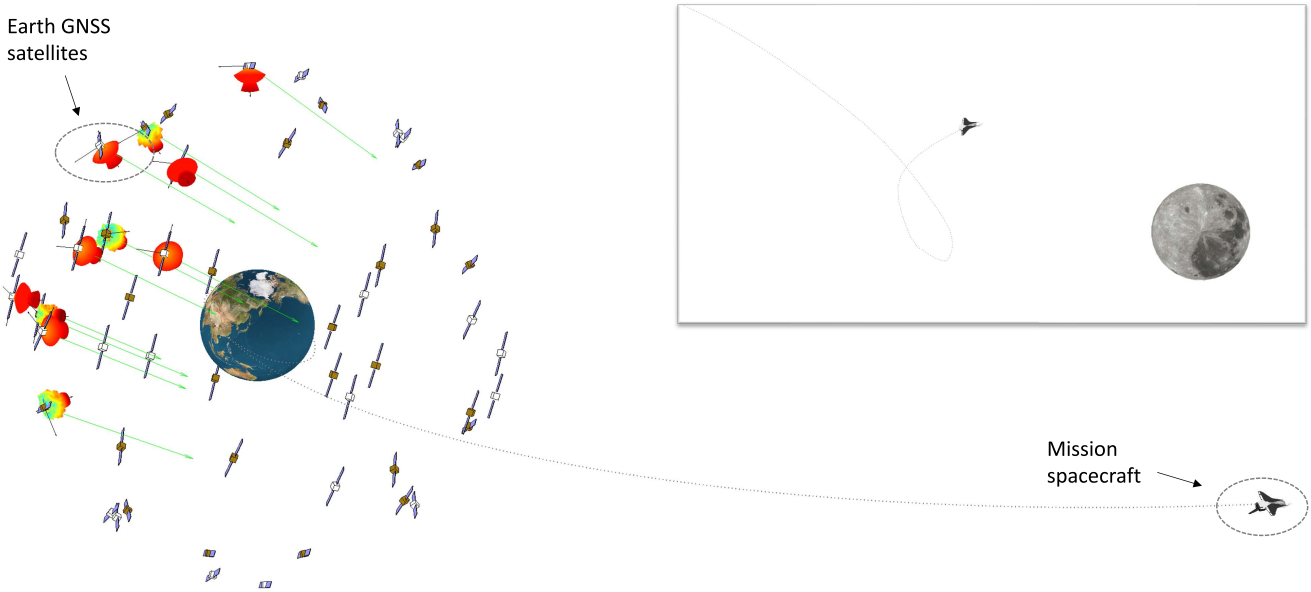

Fig. 2. Snapshot of the mission-case scenario as reproduced by the custom MATLAB ®-based mission planner and GNSS constellation simulator. Transmit-antenna radiation patterns are shown for satellites in radiometric visibility from the spacecraft. Vectors pointing towards the spacecraft are shown as well.

As a further cross-validation step, the diagonal elements in (33) can be equivalently derived from the uncertainty computation in [38].

IV. Simulation Framework

By taking the LuGRE mission-case scenario as reference for GNSS-based PNT along MTOs, a custom MATLAB ®-based mission planner and constellation simulator has been developed which duly models the GNSS signal environment experienced by an orbiting probe throughout the Earth-Moon transfer up to Moon altitude. Fig. 2 shows a snapshot of the considered mission scenario as faithfully reproduced in the dedicated software simulator. Two GNSS constellations are modeled: GPS and Galileo. As regards the former, the 3D transmit-antenna patterns for Block IIR and IIR-M satellites have been designed following the technical documentation released by the U.S. Coast Guard Navigation Center (NAVCEN) [39]. Moreover, details about the panel pattern specification for Block IIF over L1-band were retrieved based on the published scientific products from NASA's GPS Antenna Characterization Experiment (GPS ACE) [40]. Concerning Galileo satellites' antenna radiation patterns, the details of which are kept confidential, unofficial Effective Isotropic Radiated Power (EIRP) values have been assumed for main and side lobes as derived by the European Space Operations Centre (ESOC) to enable preliminary scientific investigations in support of the PROBA-3 mission [41]. A 90° off-boresight angle mask is adopted for the radiation patterns of both GNSS constellations.

A. Modeling and Simulation of GNSS Observables

In the developed constellation simulator, the synthetic generation of GNSS observables for each of the modeled GPS and Galileo satellites is bound to both *geometric* and *radiometric* visibility constraints. In particular, geometric visibility takes into account the instantaneous availability of a Line-of-Sight (LOS) link between the orbiting probe and each satellite vehicle; this LOS is obstructed either in case the satellite-spacecraft baseline is more than 90° off-boresight the nadir pointing direction, or as a result of occultation effects induced by the modeled Earth and Moon bodies. Radiometric visibility, which strictly depends on the alignment between the antenna radiation patterns of the receiver and the GNSS satellites, is assessed upon the estimation of the received Carrier-to-Noise-density ratio (C/N_0) from each satellite. This estimation is based on a link-budget model obtained through a high-accuracy fit of the expected C/N_0 levels for the LuGRE receiver throughout the mission [22]. It should be noted that the aforementioned criteria for the synthetic generation of GNSS observables overlook any peculiar conditions for which atmospheric propagation bending may induce radiometric visibility for satellites that are not visible geometrically due to Earth occlusion.

Pseudorange measurements carry satellites-to-spacecraft range information corrupted by satellite clock errors, propagation delays induced by the atmosphere, and other unmodelled effects usually lumped into a residual error term [42]. Only code-based ranging is considered for simulation purposes, and compensation of the modeled bias contributions is assumed. Therefore, the corrected pseudorange measurement to a visible satellite s at time instant t_k is simulated according to:

$$P_{r,k}^{(s)} = \rho_{r,k}^{(s)} + \underbrace{c\delta t_{r,k}}_{b_k} + \epsilon_{r,k}^{(s)} \tag{35}$$

where:

- $\rho_{r,k}^{(s)}$ is the spacecraft-to-satellite geometric range in (m);
- $\delta t_{r,k}$ is the spacecraft GNSS receiver clock offset in (s);

- $\epsilon_{r,k}^{(s)} \sim \mathcal{N}(0, \sigma_{\epsilon_{r,k}}^{(s)})$ is the normally distributed pseudorange residual in (m).

For $\delta t_{r,k}$, the apex (s) is omitted in (35) under the hypothesis that satellite measurements are predicted forward to a time of arrival common to all active receiver tracking channels (i.e., t_k); it follows that the receiver clock bias evenly affects all the available observables. Accounting for the phase noise on the clock offset and the random walk of the receiver clock drift over Δt, $\delta t_{r,k}$ is simulated according to:

$$\delta t_{r,k} = \underbrace{\sqrt{\frac{S_{c\phi}}{\Delta t} + \frac{S_{cf}\Delta t}{3}}}_{\bar{\boldsymbol{x}}_{\phi,rms}} + \mathcal{N}\left(0, S_{cf}\Delta t\right) \tag{36}$$

where $\bar{\boldsymbol{x}}_{\phi,rms}$ is the average Root-Mean-Square (RMS) value for the clock offset phase noise. As concerns $\epsilon_{r,k}^{(s)}$, the value of $\sigma_{\epsilon_{r,k}}^{(s)}$ is computed as a function of the estimated C/N_0 following the model reported in [23].

The corrected Doppler-shift measurement, transformed into the equivalent pseudorange-rate, to a visible satellite s at time instant t_k is constructed based on the radial component of the satellite-spacecraft relative velocity vector:

$$\dot{P}_{r,k}^{(s)} = \boldsymbol{u}_{r,k}^{(s)^T}\left[\dot{\boldsymbol{r}}_k^{(s)} - \dot{\boldsymbol{r}}_k\right] + \dot{b}_k + \dot{\epsilon}_{r,k}^{(s)} \tag{37}$$

where:

- $\dot{\boldsymbol{r}}_k^{(s)}$ is the velocity vector of visible satellite (s) at the measured transmission time (w.r.t. t_k) in (m/s);
- $\boldsymbol{u}_{r,k}^{(s)}$ is the spacecraft-to-satellite unit LOS vector;
- $\dot{\epsilon}_{r,k}^{(s)}$ is the normally distributed pseudorange-rate residual (i.e., $\dot{\epsilon}_{r,k}^{(s)} \sim \mathcal{N}(0, \sigma_{\dot{\epsilon}_{r,k}}^{(s)})$) in (m/s).

Similarly to $\epsilon_{r,k}^{(s)}$, the value of $\sigma_{\dot{\epsilon}_{r,k}}^{(s)}$ is retrieved as a function of the estimated C/N_0 following the corresponding model in [23].

B. Reference Trajectory and Aiding Model

Concerning the reference trajectory employed in the analyzed mission scenario, the custom constellation simulator leverages a pre-launch OD design of the LuGRE payload available as a byproduct of ongoing research activities. Although the specific details of the orbit ephemeris are kept confidential, this design fits specific requirements regarding tracking schedules, maneuver-recovery schedules, and spacecraft ground-tracking considerations. About motion dynamics, physics-based perturbation techniques are leveraged to numerically integrate non-linear differential equations of spacecraft motion starting from an initial estimate of the kinematic state. In particular, the OD design accounts for gravitational effects from Earth, Sun, and Moon, third-body perturbation effects, atmospheric drag, solar radiation pressure, and additional higher-order effects.

Starting from this reference orbit, aiding observations in terms of discrete-time spacecraft kinematics are constructed by accounting for a time-variant bias component and noise. Introducing a bias component in the model for simulated aiding observations is meant to capture discrepancies between the GNSS observations and the integrated aiding observations. Usually, a mismatch raises as a temporal offset due to asynchronous aiding data integration in the filter. Suppose the aiding observations are given as a discrete-time sequence of kinematic states. At time instant t_k and in the absence of any additional timing information, there is no apparent rationale to drive the selection of the aiding observation sample from the discrete sequence. In this regard, there is no guarantee that sample identification based on aligning the discrete timestamps brings to optimal aiding integration [43].

Specifically, the aiding observation model employed in the custom simulator can be formulated at t_k as:

$$\tilde{\boldsymbol{z}}_k = \underbrace{[\boldsymbol{r}_k\ \dot{\boldsymbol{r}}_k]^T}_{\boldsymbol{x}_k} + \tilde{\boldsymbol{b}}_k \tag{38}$$

where $\boldsymbol{x}_k$ embeds the instantaneous kinematic state (i.e., position and velocity) of the spacecraft according to the pre-launch orbit design and $\tilde{\boldsymbol{b}}_k$ is the introduced bias factor. For the latter quantity, a time-series is simulated as first-order autoregressive AR(1) process [44]:

$$\tilde{\boldsymbol{b}}_k = -\boldsymbol{A}_k\tilde{\boldsymbol{b}}_{k-1} + \boldsymbol{\eta}_k \tag{39}$$

where $\boldsymbol{A}_k$ is the diagonal matrix of process coefficients; it is defined as:

$$\boldsymbol{A}_k = (-1)\cdot\begin{bmatrix}\dot{\boldsymbol{r}}_k & \boldsymbol{0}_{3\times3}\\ \boldsymbol{0}_{3\times3} & \ddot{\boldsymbol{r}}_k\end{bmatrix} \tag{40}$$

$\dot{\boldsymbol{r}}_k$ and $\ddot{\boldsymbol{r}}_k$ being the instantaneous spacecraft velocity and acceleration states, respectively. Moreover, $\boldsymbol{\eta}_k$ is the normally distributed driving noise term with steady-state variance-covariance $\tilde{\boldsymbol{\Sigma}}_k$. Expanding upon the asynchronous mismatching behavior captured by the AR(1) process, this driving noise term allows to account for unpredictable effects such as abrupt thrusting maneuvers or temporary disturbances from other celestial bodies (e.g., space-weather phenomena) that are likely to take place during the mission.

V. Results

In this section, the simulation framework in Section IV is exploited for a twofold purpose. On the one hand, it is used to carry out analysis tasks regarding the availability of GNSS observations and satellite distribution relative to the entire span of the planned probe orbit for the LuGRE payload. On the other hand, a thorough analysis of the filtered solutions from either TA-EKF variants is meant to assess the achievable accuracy performance when GNSS-based OD is performed according to a kinematic approach.

A. Predicted Visibility and Dilution of Precision

Taking a reference C/N_0 threshold of 23 dBHz, Fig. 3(a) reports the predicted signal availability relative to modeled GPS and Galileo satellites as a function of the distance from the Earth (in RE). In particular, composite and disjoint trends are shown for the involved GNSS constellations. GNSS observables are available if both geometric and radiometric visibility are experienced at the receiver location. Line markers represent the average number of GNSS satellites under radiometric visibility measured over 15-minutes long time windows during the simulated mission transit phase. Moreover, background markers highlight that instantaneous

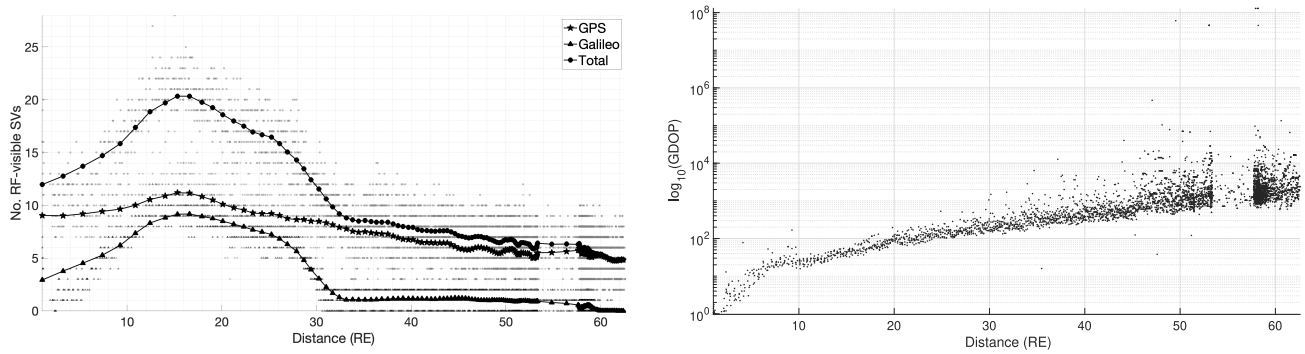

(a) (b)

Fig. 3. Expected radiometric visibility pattern for both GPS and Galileo constellations (a) and GDOP profile (b) along the MTO up to low-lunar orbit.

satellite visibility might fluctuate besides the mean expected radiometric visibility. On average, the Galileo constellation shows a much earlier radiometric visibility drop-off at about 30 RE compared to the GPS constellation. This phenomenon is likely induced by an overly pessimistic assumption for the EIRP values of both main and side lobes in Galileo transmit-antenna patterns.

The estimated GDOP profile along the MTO is represented in Fig. 3(b). Unsurprisingly, the more the spacecraft gets away from the Earth's surface, the more the GDOP deteriorates. Close to the Earth, radiometric-visible satellites fall under a broader angle of view, which generally guarantees a low linear dependency among the spacecraft-to-satellite unit LOS pointing vectors; on the contrary, getting away from the Earth's surface, the angle of view increasingly narrows whichever the satellite distribution is, and the geometrical arrangement of ranging sources deteriorates. This phenomenon is summarized by the resulting GDOP profile, which acts as a compact, although non-exhaustive, scalar indicator of the satellites' spatial distribution effect on the covariance statistics characterizing the navigation solution.

B. EKF-Based Kinematic POD With Aiding Integration

To assess the proposed TA-EKF architectures, a 15-minutes long orbital section is selected in a neighborhood of a point belonging to the planned LuGRE trajectory at a distance of 25.05 RE (i.e., 159768.9 km); the selected distance is relevant to the mission scientific objectives [24]. In order to gather significant accuracy statistics to characterize the filtered navigation solution, a sample of e3 MC realizations is collected of the aforementioned orbital segment. For each MC trial, the initial value for the AR(1) bias process is determined as a probabilistic outcome:

$$\tilde{\boldsymbol{b}}_0 \sim \mathcal{N}\left(\mathbf{0}_{6\times 1}, \begin{bmatrix} \sigma_p^2 \boldsymbol{I}_{3\times 3} & \mathbf{0}_{3\times 3} \\ \mathbf{0}_{3\times 3} & \sigma_v^2 \boldsymbol{I}_{3\times 3} \end{bmatrix}\right) \tag{41}$$

where $\sigma_v = 0.01 m/s$ and $\sigma_p = e - 2\ ms$. Moreover, a GNSS-based kinematic OD solution via standalone EKF architecture is taken as a benchmark to measure the achievable accuracy gain via the integration of aiding observations.

Fig. 4 illustrates the empirical Cumulative Density Function (eCDF) lines relative to the positioning error; in addition,

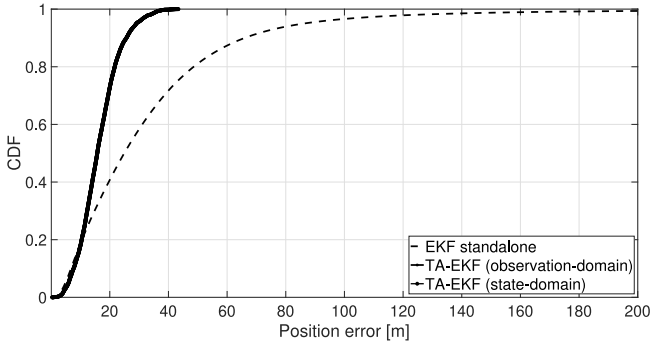

Fig. 4. Position error statistics in terms of empirical cumulative density function for both observation-domain and state-domain TA-EKF architectures. The EKF-based filtered navigation solution is taken as benchmark for performance evaluation.

summary cumulative error statistics at relevant percentiles are listed in Table I. Yet, positioning accuracy and precision analysis for the considered filtering-based algorithms are reported as box plots in Fig. 5(d). Each subplot of Fig. 5(d) shows a time series of box plots for each of the investigated filtering algorithms observed every 17 s over the whole orbital segment. In particular, each box represents the summary positioning error statics as the instantaneous output of the collected MC sample from e3 runs. The top and bottom edges of the box (i.e., the interquartile range) indicate the 75-th and 25-th percentiles, respectively, and the black mark with a square shape inside the interquartile range identifies the mean of the MC sample. The lines extending above and below each box are referred to as whiskers. The latter goes from the end of the interquartile range to the furthest MC realization within the whisker length. Observations beyond the whisker length are marked as outliers and relevant to characterizing the instantaneous position estimation uncertainty. The proposed TA-EKF designs for aiding integration pursue nearly equivalent OD performance, being the corresponding eCDF lines overlapped. A further manipulation of the filtering equations using the information form [45] can effectively highlight the duality between the two architectures. However, implementation discrepancies are currently under investigation and will be addressed in future work.

TABLE I
CUMULATIVE POSITION ERROR STATISTICS (ECDF PERCENTILE) FOR EITHER TA-EKF ARCHITECTURES AND THE STANDALONE EKF MEASURED OVER THE ANALYZED 15-MINUTES LONG MTO SEGMENT

Navigation Filter	CDF (percentile)			
	25	50	75	95
EKF standalone	12.583	24.928	43.073	86.199
TA-EKF (observation-domain)	11.455	15.734	20.445	29.053
TA-EKF (state-domain)	11.457	15.731	20.448	29.056

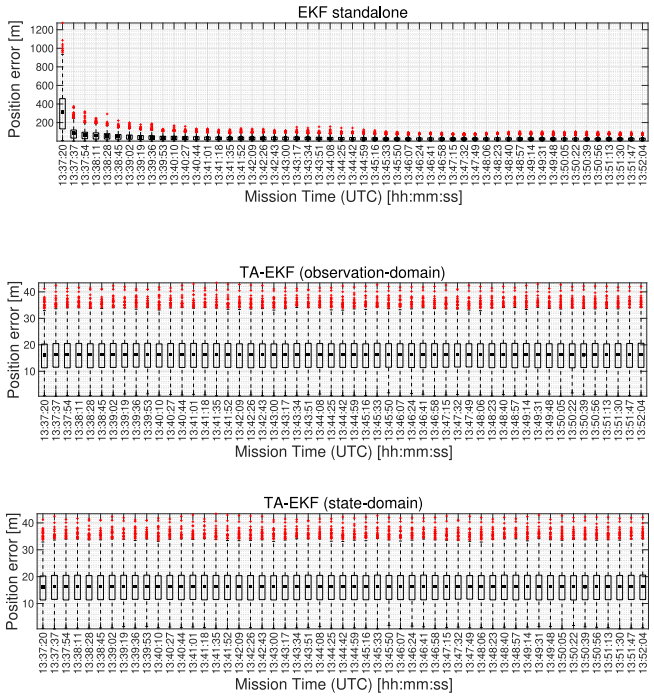

Fig. 5. Statistical characterization of the OD solution for both observation-domain and state-domain TA-EKF architectures and for a standalone EKF model. UTC timestamps are referred to a simulated orbit reflecting the analyzed mission scenario.

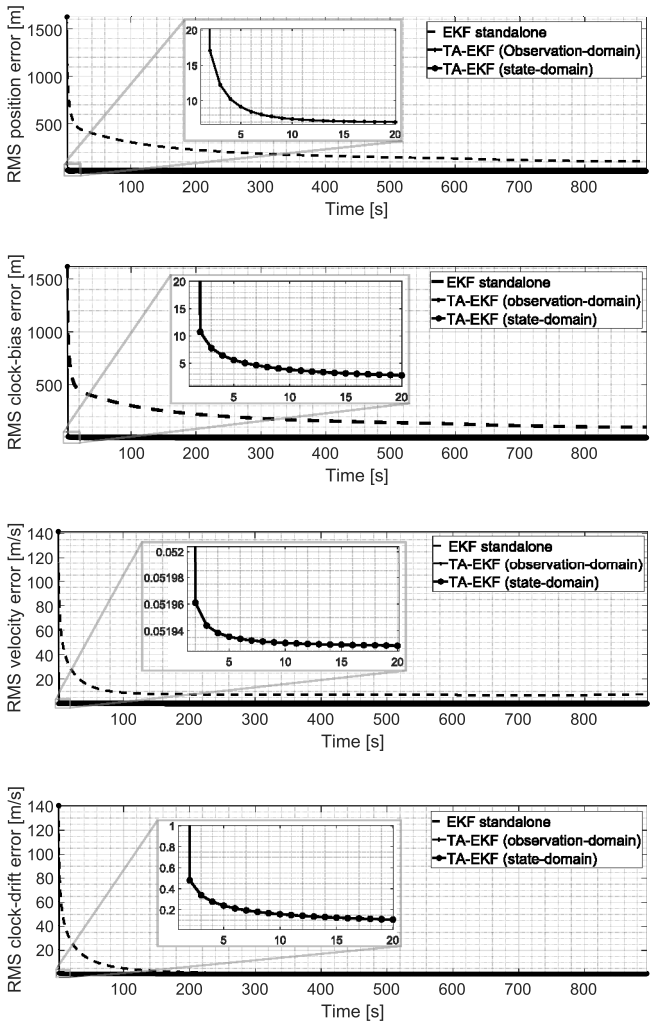

Fig. 6. RMS state covariance statistics (1σ) relative to the position, velocity, clock-bias and clock-drift states. Comparison between the proposed TA-EKF models. The standalone EKF is taken as benchmark for performance evaluation.

For the standalone EKF, the vulnerability of a kinematic approach to OD is rather obvious. This filtering architecture interpolates between successive position-fixing epochs through a simplistic dynamical model and heavily relies on GNSS observations to estimate the spacecraft orbit. However, the adverse space environment limits the accuracy of satellite-based ranging measurements. Moreover, the geometrical arrangement of satellite-based ranging sources exacerbates the propagation of measurement errors over the computed orbit position (the reader can refer to Fig. 3(b) to visualize the detrimental GDOP conditions predicted for the LuGRE Earth-Moon transfer). These effects are successfully mitigated via the integration of aiding observations, which allow the flaws of the kinematic approach to be overcome to a large extent. As a matter of fact, the developed TA-EKF models pursue remarkable accuracy compared to the standalone algorithm. According to Table I, the position accuracy improvement measured at the 50-th percentile amounts to 36.88%, while at the 95-th percentile it increases to 66.29%. Moreover, by looking at Fig. 4, the maximum positioning error measured for the aided architectures is bound to 43.48 m as opposed to the much higher error of 1272.57 m measured for the standalone solution. Correspondingly, it is clear from Fig. 5(d) that the position estimation uncertainty is consistently reduced via the proposed TA-EKF variants with error outliers limited to about 40 m.

Fig. 6(e) highlights the convergence pattern (1σ-uncertainty) of the navigation filter estimates for the process states modeled in (12). Owing to spacecraft dynamics, the process state estimate suffers the adoption of a constant velocity approximation (i.e., high acceleration noise) for the unaided EKF. Therefore, upon a coarser linearization of the state-transition model w.r.t. the one attainable with the true (but unknown) state, the gradient of $\boldsymbol{f}_{k-1}$ over the uncertainty bounds of the state-estimate is likely to be significant; this condition, in turns, negatively impacts on the process state estimate. Moreover, such a phenomenon reflects on the process covariance estimate, which depends upon the state estimate as a consequence of linearization. Upon integration of aiding

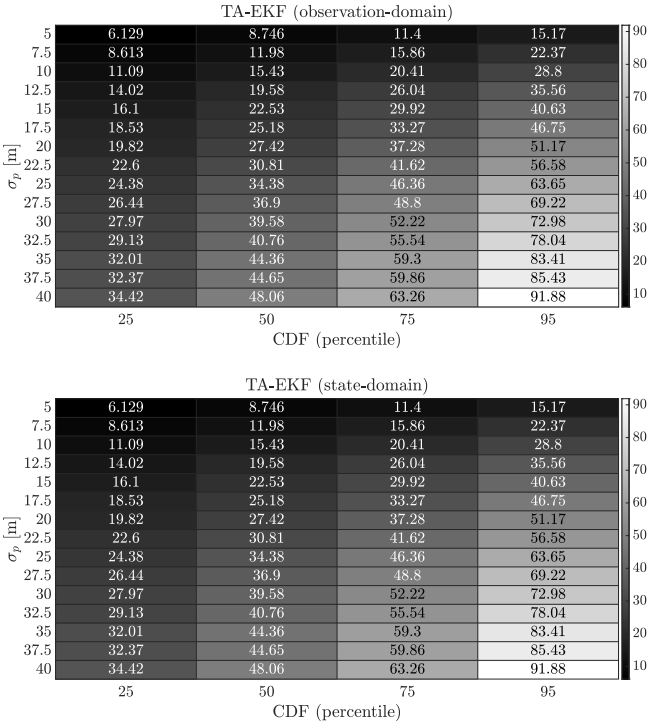

Fig. 7. Heatmap chart of position error statistics (percentiles) for different variances of the multivariate normal distribution used to probabilistically draw the AR (1) bias process initial value. Map cells are measured positioning errors for both observation-domain (top chart) and state-domain (bottom chart) TA-EKF architectures.

observations, the TA-EKF state-estimate benefits from a finer state-space model linearization. As a result, the estimator trusts the navigation solution more, and this is visible from the overlapping RMS curves of both TA-EKF models.

Eventually, the heatmap charts in Fig. 7(c) illustrate relevant percentiles of cumulative error statistics against different values of the second-order central moment for the multivariate Gaussian distribution used to draw MC samples of AR(1) bias initial values. Each cell in the map represents the 3D position error for both observation-domain (top chart) and state-domain (bottom chart) TA-EKF implementations. These results confirm again the similarity between the two implementations. Starting from a set of mission requirements in terms of accuracy for the OD task agreed upon pre-launch mission phase, the scope of the proposed analysis is to provide valuable guidelines in support of the prospective design of a TA-EKF-based navigation unit implementing kinematic OD. This heatmap allows the translation of OD requirements into precision and accuracy criteria to be satisfied upon the design of a pre-launch orbital model aiding observation can be retrieved from.

VI. Conclusion

As interest and investment are steadily growing in space exploration missions, GNSS is an attractive technology for OD, allowing increased autonomy and reducing the burden of ground-based tracking operations. In the framework of the upcoming LuGRE demonstration mission for GNSS-based PNT in cis-lunar space and at moon altitudes, aided EKF-based solutions for kinematic OD have been investigated [46], [47]. Under the operational assumption that the receiver does not interface with the spacecraft GNC subsystem, this paper has proposed two alternative yet equivalent designs of a TA-EKF model; these architectures integrate aiding information in the form of kinematic observations of the planned spacecraft trajectory retrieved from a pre-launch orbit design. By leveraging MC analyses to draw significant statistics, the present study has demonstrated that either TA-EKF architectures can pursue remarkable accuracy in the OD task with promising robustness to detrimental GDOP fluctuations and satellite signal depletion. Compared to a standalone EKF architecture, the accuracy of the filtered positioning solution can be enhanced up to 66.29% at the 95-th percentile. Moreover, filter convergence is improved against the standalone counterpart in both position and velocity states. Recognizing the challenges of asynchronous aiding data integration and the pitfalls of misspecified statistics for aiding observations, the upcoming research will devote effort to developing techniques that can enhance the reliability and robustness of the filtered navigation solution.

Appendix

Hereinafter it is considered the computation of the covariance of a common mean estimator of two multivariate normal distributions with the same mean and different variance-covariance matrices. The BLUE of such common mean is defined as [48]:

$$\hat{\boldsymbol{x}}_k^{BLUE} = \left[\left(\boldsymbol{P}_k^-\right)^{-1} + \tilde{\boldsymbol{P}}_k^{-1}\right]^{-1}\left[\left(\boldsymbol{P}_k^-\right)^{-1}\boldsymbol{\Phi}_{k-1}\hat{\boldsymbol{x}}_{k-1} + \tilde{\boldsymbol{P}}_k^{-1}\tilde{\boldsymbol{x}}_k\right]. \tag{42}$$

To compute its covariance, it is worth resorting to the uncertainty propagation principle for linear combinations. Specifically, if $\boldsymbol{\Sigma}_{\boldsymbol{x}}$ and $\boldsymbol{\Sigma}_{\boldsymbol{y}}$ are, respectively, the covariance matrices of two random vectors $\boldsymbol{x}$ and $\boldsymbol{y}$, and they are related by $\boldsymbol{y} = \boldsymbol{A}\boldsymbol{x}$, the identity

$$\boldsymbol{\Sigma}_{\boldsymbol{y}} = \boldsymbol{A}\boldsymbol{\Sigma}_{\boldsymbol{x}}\boldsymbol{A}^T \tag{43}$$

holds [49]. Moreover, if $\boldsymbol{x}$ and $\boldsymbol{y}$ are independent, the covariance of their weighted sum $\boldsymbol{z} = \boldsymbol{A}\boldsymbol{x} + \boldsymbol{B}\boldsymbol{y}$ is

$$\boldsymbol{\Sigma}_{\boldsymbol{z}} = \boldsymbol{\Sigma}_{\boldsymbol{A}\boldsymbol{x}} + \boldsymbol{\Sigma}_{\boldsymbol{B}\boldsymbol{y}}. \tag{44}$$

Using (43) and (44), and therefore assuming independence among the random vectors $\boldsymbol{\Phi}_{k-1}\hat{\boldsymbol{x}}_{k-1}$ and $\tilde{\boldsymbol{x}}_k$, we can propagate their respective covariances within (26). The resulting covariance of the common mean estimator $\hat{\boldsymbol{x}}_k^{BLUE}$ is

$$\boldsymbol{P}_k^{BLUE} = \left\{\left(\boldsymbol{P}_k^-\right)^{-1} + \tilde{\boldsymbol{P}}_k^{-1}\right\}^{-1}\left\{\left(\boldsymbol{P}_k^-\right)^{-1}\boldsymbol{P}_k^-\left[\left(\boldsymbol{P}_k^-\right)^{-1}\right]^T \tag{45}$$

$$+ \tilde{\boldsymbol{P}}_k^{-1}\tilde{\boldsymbol{P}}_k\left(\tilde{\boldsymbol{P}}_k^{-1}\right)^T\right\}\left\{\left[\left(\boldsymbol{P}_k^-\right)^{-1} + \tilde{\boldsymbol{P}}_k^{-1}\right]^{-1}\right\}^T \tag{46}$$

$$= \left\{\left(\boldsymbol{P}_k^-\right)^{-1} + \tilde{\boldsymbol{P}}_k^{-1}\right\}^{-1}\left\{\left[\left(\boldsymbol{P}_k^-\right)^{-1}\right]^T \tag{47}$$

$$+ \left(\tilde{\boldsymbol{P}}_k^{-1}\right)^T\right\}\left\{\left[\left(\boldsymbol{P}_k^-\right)^{-1} + \tilde{\boldsymbol{P}}_k^{-1}\right]^{-1}\right\}^T \tag{48}$$

$$= \left\{ \left(\boldsymbol{P}_k^-\right)^{-1} + \tilde{\boldsymbol{P}}_k^{-1} \right\}^{-1} \left\{ \left[\left(\boldsymbol{P}_k^-\right)^{-1} \right]^T \right. \tag{49}$$

$$\left. + \left(\tilde{\boldsymbol{P}}_k^{-1}\right)^T \right\} \left\{ \left[\left(\boldsymbol{P}_k^-\right)^{-1} \right]^T + \left(\tilde{\boldsymbol{P}}_k^{-1}\right)^T \right\}^{-1} \tag{50}$$

$$= \left\{ \left(\boldsymbol{P}_k^-\right)^{-1} + \tilde{\boldsymbol{P}}_k^{-1} \right\}^{-1} \tag{51}$$

where we used $(\boldsymbol{A}^{-1})^T = (\boldsymbol{A}^T)^{-1}$, $\boldsymbol{A}^{-1}\boldsymbol{A} = \boldsymbol{I}$, and $(\boldsymbol{A}+\boldsymbol{B})^T = (\boldsymbol{A}^T + \boldsymbol{B}^T)$, being $\boldsymbol{A}$ and $\boldsymbol{B}$ square, invertible matrices.

REFERENCES

[1] W. P. Birmingham, B. L. Miller, and W. L. Stein, "Experimental results of using the GPS for landsat 4 onboard navigation," *Navigation*, vol. 30, no. 3, pp. 244–251, 1983.

[2] T. G. Reid et al., "Navigation from low earth orbit," in *Position, Navigation, and Timing Technologies in the 21st Century*, Hoboken, NJ, USA: Wiley, 2020, pp. 1359–1379.

[3] "The interoperable global navigation satellite systems space service volume," in *United Nations Digital Library*, United Nat. Office Outer Space Aff., Vienna, VA, USA, Oct. 2018.

[4] J. L. Burch, T. E. Moore, R. B. Torbert, and B. L. Giles, "Magnetospheric multiscale overview and science objectives," *Space Sci. Rev.*, vol. 199, no. 1, pp. 5–21, Mar. 2016.

[5] D. Baird, *Record-Breaking Satellite Advances NASA's Exploration of High-Altitude GPS*, 2019, Accessed: Nov. 23, 2022. [Online]. Available: www.nasa.gov

[6] L. Iess, M. Di Benedetto, N. James, M. Mercolino, L. Simone, and P. Tortora, "Astra: Interdisciplinary study on enhancement of the end-to-end accuracy for spacecraft tracking techniques," *Acta Astronautica*, vol. 94, no. 2, pp. 699–707, 2014.

[7] E. Turan, S. Speretta, and E. Gill, "Performance analysis of crosslink radiometric measurement based autonomous orbit determination for cislunar small satellite formations," *Adv. Space Res.*, vol. 72, no. 7, pp. 2710–2732, 2022.

[8] O. Montenbruck, E. Gill, and F. Lutze, "Satellite orbits: Models, methods, and applications," *Appl. Mech. Rev.*, vol. 55, no. 2, pp. B27–B28, 2002.

[9] S. K. Biswas and H. B. Hablani, "Ground based navigation of spacecraft in lunar transfer trajectory, with application to Chandrayaan-2," in *Proc. Memorial Symp. Estimat., Navigat. Spacecraft Control*, 2015, pp. 371–390.

[10] S. Bhaskaran, "Autonomous navigation for deep space missions," in *Proc. SpaceOps*, 2012, Art. no. 1267135.

[11] E. Turan, S. Speretta, and E. Gill, "Autonomous navigation for deep space small satellites: Scientific and technological advances," *Acta Astronautica*, vol. 193, pp. 56–74, Apr. 2022.

[12] *The Global Exploration Roadmap*, Int. Space Explor. Coordinat. Group, Berlin, Germany, 2018.

[13] L. Musumeci, F. Dovis, J. S. Silva, P. F. da Silva, and H. D. Lopes, "Design of a high sensitivity GNSS receiver for Lunar missions," *Adv. Space Res.*, vol. 57, no. 11, pp. 2285–2313, Jun. 2016.

[14] N. Witternigg et al., "Weak GNSS signal navigation for Lunar exploration missions," in *Proc. 28th Int. Tech. Meet. Satel. Div. Inst. Navigat. (ION GNSS+ 2015)*, 2015, pp. 3928–3944.

[15] V. Capuano, C. Botteron, J. Leclère, J. Tian, Y. Wang, and P.-A. Farine, "Feasibility study of GNSS as navigation system to reach the Moon," *Acta Astronautica*, vol. 116, pp. 186–201, Dec. 2015.

[16] S. Molli et al., "Navigation performance of low lunar orbit satellites using a Lunar radio navigation satellite system," in *Proc. 36th Int. Tech. Meet. Satel. Div. Inst. Navigat. (ION GNSS+ 2023)*, 2023, pp. 4051–4083.

[17] C. Mehlen and D. Laurichesse, "Improving GPS navigation with orbital filter," in *Spacecraft Guidance, Navigation and Control Systems*, vol. 425, B. Schürmann, Ed. Paris, France: ESA Special Publ., Feb. 2000, p. 123.

[18] V. Capuano, "GNSS-based orbital filter for earth moon transfer orbits," *J. Navigat.*, vol. 69, no. 4, pp. 745–764, 2015.

[19] O. Montenbruck, T. Van Helleputte, R. Kroes, and E. Gill, "Reduced dynamic orbit determination using GPS code and carrier measurements," *Aerosp. Sci. Technol.*, vol. 9, no. 3, pp. 261–271, 2005.

[20] T. P. Yunck et al., "First assessment of GPS-based reduced dynamic orbit determination on TOPEX/Poseidon," *Geophys. Res. Lett.*, vol. 21, no. 7, pp. 541–544, 1994.

[21] V. Capuano, E. Shehaj, P. Blunt, C. Botteron, and P.-A. Farine, "An adaptive GNSS-based reduced dynamic approach for real time autonomous navigation from the earth to the moon," in *Proc. Pac. PNT Meet.*, 2017, pp. 331–347.

[22] J. J. Parker et al., "The Lunar GNSS receiver experiment (LuGRE)," in *Proc. Int. Tech. Meet. Inst. Navigat. (ION ITM 2022)*, 2022, pp. 420–437.

[23] L. Konitzer, N. Esantsi, and J. Parker, "Navigation performance analysis and trades for the Lunar GNSS receiver experiment (LuGRE)," in *Proc. AAS/AIAA Astrodyn. Spec. Conf.*, 2022, pp. 1–12.

[24] A. Minetto, F. Dovis, A. Nardin, O. Vouch, G. Impresario, and M. Musmeci, "Analysis of GNSS data at the Moon for the LuGRE project," in *Proc. IEEE 9th Int. Workshop Metrol. Aerosp. (MetroAeroSpace)*, 2022, pp. 134–139.

[25] A. Nardin, A. Minetto, O. Vouch, M. Maiani, and F. Dovis, "Snapshot acquisition of GNSS signals in space: A case study at Lunar distances," in *Proc. 35th Int. Tech. Meet. Satel. Div. Inst. Navigat. (ION GNSS+ 2022)*, Denver, Colorado, 2022, pp. 3603–3617.

[26] A. Nardin, A. Minetto, S. Guzzi, F. Dovis, L. Konitzer, and J. J. K. Parker, "Snapshot tracking of GNSS signals in space: A case study at lunar distances," in *Proc. 36th Int. Tech. Meet. Satel. Div. Inst. Navigat. (ION GNSS+ 2023)*, Denver, Colorado, 2023, pp. 3267–3281.

[27] D. Švehla and M. Rothacher, "Kinematic precise orbit determination for gravity field determination," in *Proc. Int. Assoc. Geodesy IAG Gener. Assembly*, Sapporo, Japan, 2005, pp. 181–188.

[28] O. Vouch, A. Nardin, A. Minetto, M. Valvano, S. Zocca, and F. Dovis, "A customized EKF model for GNSS-based navigation in the harsh space environment," in *Proc. IEEE Int. Conf. Wireless Space Extreme Environ. (WiSEE)*, 2023, pp. 13–18.

[29] R. Brown and P. Hwang, *Introduction to Random Signals and Applied Kalman Filtering with Matlab Exercises*. Hoboken, NJ, USA: Wiley, 2012.

[30] O. Vouch, A. Minetto, G. Falco, and F. Dovis, "Enhanced Bayesian state space estimation for a GNSS/INS tightly-coupled integration in harsh environment: An experimental study," in *Proc. 34th Int. Tech. Meet. Satel. Div. Inst. Navigat. (ION GNSS+ 2021)*, 2021, pp. 3368–3381.

[31] O. Vouch, A. Minetto, G. Falco, and F. Dovis, "On the adaptivity of unscented particle filter for GNSS/INS tightly-integrated navigation unit in urban environment," *IEEE Access*, vol. 9, pp. 144157–144170, 2021.

[32] P. Groves, *Principles of GNSS, Inertial, and Multisensor Integrated Navigation Systems*, 2nd ed. London, U.K.: Artech House, 2013.

[33] R. G. Brown and P. Y. Hwang, *Introduction to Random Signals and Applied Kalman Filtering*, New York, NY, USA: Wiley Inc., 1992.

[34] D. A. Vallado, R. S. Hujsak, T. M. Johnson, J. H. Seago, and J. W. Woodburn, "Orbit determination using ODTK version 6," in *Proc. Eur. Space Astron. Centre*, Madrid, Spain, 2010, pp. 3–6.

[35] W.-L. Loh, "Estimating the common mean of two multivariate normal distributions," *Annal. Statist.*, vol. 19, no. 1, pp. 297–313, 1991.

[36] D. Zhuang, S. E. Ahmed, S. Liu, and T. Ma, *Estimation of the Common Mean of Two Multivariate Normal Distributions Under Symmetrical and Asymmetrical Loss Functions*, Cham, Switzerland: Springer, 2020, pp. 351–373.

[37] K. Krishnamoorthy, "Estimation of a common multivariate normal mean vector," *Annal. Inst. Statist. Math.*, vol. 43, no. 4, pp. 761–771, Dec. 1991.

[38] P. R. Bevington and D. K. Robinson, *Data Reduction and Error Analysis for the Physical Sciences*, 3rd ed. New York, NY, USA: McGraw-Hill, 2003, pp. 56–57.

[39] W. A. Marquis and D. L. Reigh, "The GPS block IIR and IIR-M broadcast L-band antenna panel: Its pattern and performance," *Navigation*, vol. 62, no. 4, pp. 329–347, 2015.

[40] J. E. Donaldson, J. J. Parker, M. C. Moreau, D. E. Highsmith, and P. D. Martzen, "Characterization of on-orbit GPS transmit antenna patterns for space users," *Navigation*, vol. 67, no. 2, pp. 411–438, 2020.

[41] W. Enderle, F. Gini, S. Erik, and M. Volker,, "PROBA-3 precise orbit determination based on GNSS observations," in *Proc. 32nd Int. Tech. Meet. Satel. Div. Inst. Navigat. (ION GNSS+ 2019)*, 2019, pp. 1187–1198.

[42] P. Teunissen and O. Montenbruck, *Springer Handbook of Global Navigation Satellite Systems*, Cham, Switzerland: Springer, 2021.

[43] B.-K. Yi, H. Jagadish, and C. Faloutsos, "Efficient retrieval of similar time sequences under time warping," in *Proc. 14th Int. Conf. Data Eng.*, 1998, pp. 201–208.

[44] S. M. Kay, *Fundamentals of Statistical Signal Processing: Estimation Theory*, Upper Saddle River, NJ, USA: Prentice-Hall, Inc., 1993.

[45] Y. Bar-Shalom, X. R. Li, and T. Kirubarajan, *Estimation with Applications to Tracking and Navigation: Theory Algorithms and Software*, Hoboken, NJ, USA: Wiley, 2004.
[46] O. Vouch et al., "Bayesian integration for deep-space navigation with GNSS signals," in *Proc. 27th Int. Conf. Inf. Fusion (FUSION)*, 2024, pp. 1–8.
[47] O. Vouch et al., "Advancing autonomous navigation: GNSS-based orbit determination in deep space," in *Proc. 37th Int. Tech. Meet. Satel. Div. Inst. Navigat. (ION GNSS+ 2024)*, 2024, pp. 1–9.
[48] W.-L. Loh, "Estimating the common mean of two multivariate normal distributions," Dept. Statist., Purdue Univ.ersity, Rep. 88-48, Oct. 1988.
[49] J. Tellinghuisen, "Statistical error propagation," *J. Phys. Chem. A*, vol. 105, no. 15, pp. 3917–3921, Apr. 2001.

Oliviero Vouch (Graduate Student Member, IEEE) received the B.Sc. degree in electronics and communications engineering and the M.Sc. degree in Communications and Computer Networks Engineering from the Politecnico di Torino, Turin, Italy, in 2018 and 2020, respectively, where he is currently pursuing the Ph.D. degree with the Department of Electronics and Telecommunications. He is member of the Navigation Signal Analysis and Simulation Group. His research interests cover advanced Bayesian estimation applied to multisensor integrated navigation units based on Global Navigation Satellite System.

Andrea Nardin (Member, IEEE) received the M.Sc. degree in telecommunications engineering and the Ph.D. degree in electrical, electronics and communications engineering from the Politecnico di Torino, Turin, Italy, in 2018 and 2023, respectively. where he is currently a Postdoctoral Researcher with the Department of Electronics and Telecommunications. Since 2018, he has been working with the Navigation Signal Analysis and Simulation Group, Politecnico di Torino and in 2021, he was a Visiting Doctoral Researcher with the Information Processing Lab, Northeastern University, Boston, MA, USA. His research interests include signal processing architectures and signal design applied to GNSSs and LEO PNT.

Alex Minetto (Member, IEEE) received the B.Sc. and M.Sc. degrees in telecommunications engineering and the Ph.D. degree in electrical, electronics, and communications engineering from the Politecnico di Torino, Turin, Italy, in 2013, 2015, and 2020, respectively. He joined the Department of Electronics and Telecommunications of Politecnico di Torino in 2021, as a Researcher and an Assistant Professor. His current research interests cover navigation signal design and processing, advanced Bayesian estimation applied to positioning, navigation, and timing technologies.

Simone Zocca (Member, IEEE) received the B.Sc. degree in telecommunication engineering and the M.Sc. degree in communication and computer networks engineering from the Politecnico di Torino, Turin, Italy, in 2018 and 2020, respectively, where he is currently pursuing the Ph.D. degree within the Navigation Signal Analysis and Simulation Group with the Department of Electronics and Telecommunications. His research is focused on innovative solutions for signal processing techniques and Bayesian estimation applied to global navigation satellite system.

Matteo Valvano received the B.Sc. degree in electronics engineering and the M.Sc. degree in communications and computer networks engineering from the Politecnico di Torino, Turin, Italy, in 2020 and 2023, respectively. His thesis research centered on GNSS-based algorithms for precise orbit determination in space, during which he actively contributed to the LuGRE project in collaboration with the Navigation Signal Analysis and Simulation Group. He is currently employed as a Navigation System Engineer with Intecs, Rome, Italy.

Fabio Dovis (Member, IEEE) was born in Bruino, Italy, in 1970. He received the M.Sc. and Ph.D. degrees from the Politecnico di Torino, Turin, Italy, in 1996 and 2000, respectively. In 2004, he joined the Department of Electronics and Telecommunications, Politecnico di Torino as an Assistant Professor, where he has been a Full Professor since 2021. He coordinates the Navigation Signal Analysis and Simulation Research Group. His research interests include design of GPS and Galileo receivers and advanced signal processing for interference and multipath detection and mitigation, and also ionospheric monitoring. He is a member of the IEEE Aerospace and Electronics Systems Society Navigation Systems Panel.

Open Access funding provided by 'Politecnico di Torino' within the CRUI CARE Agreement